Available online at www.sciencedirect.com

ScienceDirect

Advances in Space Research 74 (2024) 6012–6019

ADVANCES IN SPACE RESEARCH
(a COSPAR publication)

www.elsevier.com/locate/asr

Impact of interplanetary shock on nitric oxide cooling emission: A superposed epoch study

Tikemani Bag*, Y. Ogawa

National Institute of Polar Research, 10-3, Midoricho, Tachikawa, Tokyo, Japan

Received 23 June 2024; received in revised form 30 July 2024; accepted 2 August 2024
Available online 6 August 2024

Abstract

The impact of interplanetary (IP) shock on Nitric Oxide (NO) 5.3 µm cooling emission is studied during geomagnetic quiet periods. The Active Magnetosphere and Planetary Electrodynamics Response Experiment measurements of field-aligned-currents intensify during IP shock with a relatively higher magnitude in southern hemisphere as compared to the northern hemispheric counterpart. The Defense Meteorological Satellite Program spacecraft observations displayed an early and strong enhancement in the precipitating particle flux of energy less than 1 keV. The particle flux of higher energy responds at later time. The NO density exhibited a significant, pre-event increase by an order of magnitude due to low-energy particle precipitation. The thermospheric temperature increased by about 100 K at 400 km. The superposed epoch analysis study revealed a linear enhancement in SABER (Sounding of the Atmosphere using Broadband Emission Radiometry) measurements of NO cooling emission onboard the TIMED (Thermosphere Ionosphere Mesosphere Energetics Dynamics) satellite due to the prompt increase in particle precipitations and thermospheric temperature triggered by IP shock.

Keywords: Interplanetary shock; Infrared Radiative emission; Mesosphere-Thermosphere Energetics and Dynamics; TIMED-SABER satellite; Superposed Epoch Analysis

1. Introduction

Interplanetary (IP) shock is one of the common phenomena that significantly affects the interaction between solar wind and magnetosphere. IP shock is the rapid disturbance in the solar wind characterized by abrupt changes in its speed, density, and magnetic field orientation; usually driven by coronal mass ejections (CMEs), Corotating Interaction Regions (CIRs) and/or solar flares. When a fast stream of solar wind overtakes a slower stream, it prompts the formation of IP shock (Oliveira, 2017 and references therein). The resulting abrupt changes drive shock waves that propagate through the interplanetary medium. IP shock is classified into different categories depending on the speed of the shock with respect to that of the ambient solar wind and the orientation of the interplanetary magnetic field (see Oliveira, 2017 for a review). When the shock's relative speed exceeds that of the ambient solar wind, it is called a fast shock; if it is lower, it is termed a slow shock. A fast forward shock (FFS) moves away from the sun, while a fast reverse shock moves towards the sun. During FFS events, solar wind parameters such as plasma density, magnetic field, pressure, and speed increase. FFS events are more frequent and highly geoeffective. In contrast, slow reverse shocks (SRS) result in decreased solar wind dynamic pressure and density, increased interplane-

---

* Corresponding author.
E-mail address: tikemani.bag@nipr.ac.jp (T. Bag).

https://doi.org/10.1016/j.asr.2024.08.005
0273-1177/

tary magnetic field strength, and enhanced solar wind speed.

IP shock dictates the behavior of magnetosphere-ionosphere-thermosphere (MIT) system due to its role in affecting shape, size, and orientation of the magnetosphere. Interplanetary shock triggers numerous geophysical processes, influencing areas from the magnetosphere down to the Earth's surface including field-aligned-currents (FACs), radiation belts, daytime aurora, polar vortex, total electron content and neutral atmosphere. In addition, it also drives geomagnetic storms and substorms along with the geomagnetically induced current (Burlaga, 1995; Zhou et al., 2003; Palmroth et al., 2004; Lui, 2011; Schiller et al., 2016; Belakhovsky et al., 2017; Yue et al., 2010; Lu et al., 2018; Shi et al., 2017; Shi et al., 2019; Hartinger et al., 2022; Chen et al., 2023; Bag and Ogawa, 2024a; Oliveira et al., 2024 and references therein). Oliveira and Raeder (2014) observed an increase in hot electron fluxes and intensification of electron cyclotron waves during shock events due to magnetospheric compression and subsequent particle acceleration. The sudden compression and heating of magnetospheric plasma, due to IP shocks, also leads to vortex formations in the magnetospheric and ionospheric plasma (Gkioulidou et al., 2022). These vortices transport energy and particles across different regions, affecting the overall stability and behavior of the magnetosphere-ionosphere system.

Recent studies revealed that the geoeffectiveness of IP shock strongly depends on the impact angle. Nearly frontal shock causes relatively higher intensification of field-aligned currents and induces significant changes in the radiation belts, affecting the dynamics and energetics of trapped particle populations, leading to higher energy deposition into the magnetosphere as compared to oblique shocks (Oliveira et al., 2024; Turner et al., 2021). It also results in the stronger auroral activity, ionospheric flow vortices and expands the equatorial auroral boundary through pitch angle diffusion of low-energy particle precipitation. This energy deposition alters the electron density and thermospheric temperature, and increases thermospheric density and satellite orbit drag (Rae et al., 2022; Fang et al., 2023; Cao et al., 2013; Fu et al., 2011; Shi et al., 2017; Shi et al., 2019; Yue et al., 2010; Zhou et al., 2003; Oliveira and Zesta., 2019; Liu et al., 2023). Furthermore, the impact angle of IP shocks influences the amplitude, frequency, and power spectra of ultra-low frequency (ULF) waves. More perpendicular shocks generate stronger ULF waves with higher frequencies. These ULF waves interact with charged particles, accelerating them and leading to increased ionization and heating in the upper atmosphere. This, in turn, affects radio wave propagation and satellite communications (Oliveira, 2023; Oliveira et al., 2024 and references therein).

The IP shock also increases the efficiency of solar wind-magnetosphere interaction and ionospheric convection (Boudouridis et al., 2004a,b; 2005; Connor et al., 2014; Ober et al., 2006). It shows a strong positive correlation with Joule heating rate (1992; Palmroth et al., 2004; Bag and Ogawa, 2024b). Palmroth et al. (2004), by using ACE solar wind data, the AE index, and GUMICS MHD simulations, suggested an increase in Joule heating during positive pressure impulse events. Similarly, Shi et al. (2017) observed a sudden increase in daytime, high latitude thermospheric density and downward Poynting flux during positive pressure impulse event by using OpenGGCM and multi-satellite instruments. Knipp et al. (2013) reported the damping response of thermospheric density to shock-induced geomagnetic storms due to enhanced NO production and subsequent cooling emission, highlighting the need to better understand these processes for accurate prediction of the thermospheric response to space weather events (Bowman et al., 2008). Recently, Bag and Ogawa (2024), by using a combination of model simulations and observations, revealed an enhancement in the thermospheric NO cooling emission during the IP event on November 8, 2010. They inferred that the enhancement in NO cooling emission is due to the expansion of magnetosphere and subsequent increase in Joule heating rate and particle precipitation.

Nitric Oxide (NO) radiative emission at 5.3 μm regulates thermospheric temperature increases due to its radiative properties (Mlynczak et al., 2003; Kockarts, 1980). It is a dominant coolant in the Earth's atmosphere above 100 km. It primarily results due to the inelastic collision of NO with atomic oxygen. Low-energy particle flux also contributes significantly to high latitude thermospheric NO density particularly during space weather and auroral events. Electron fluxes of 1–10 keV and ion fluxes of 10–20 keV dissociate N_2 into atomic nitrogen (N^4S, N^2D), which subsequently reacts with molecular oxygen to produce NO density (Barth, 2010; Barth et al., 2009; Richards, 2004). There are several studies on the response of NO radiative emission to geomagnetic storms (Mlynczak et al., 2003; Knipp et al., 2013; Li et al., 2018; Bharti et al., 2018; Bag., 2018a,b; Bag et al., 2020, 2023a-b; Bag and Ogawa, 2024a,b and references therein). However, there has been little attempt to understand the impacts of IP shocks on NO emission. In the present study, for the first time, we statistically investigate the impacts of IP shocks on NO cooling emission during geomagnetic quiet period by using SABER (Sounding of the Atmosphere using Broadband Emission Radiometry) measurements onboard the TIMED (Thermosphere Ionosphere Mesosphere Energetics Dynamics) satellite. We divide this study into five sections. Section 2 provides a brief introduction of the data sets and analysis method used. It also includes the various geomagnetic indices and interplanetary solar wind parameters. The corresponding response of the thermospheric NO emission to IP shock is discussed in the Section 3 and Section 4 by using model simulation and satellite observations. We conclude this paper with a summary in Section5.

2. Data analysis and method

The SABER observations of NO cooling emission onboard the TIMED satellite along with NRLMSISE2.1

model simulation of atmospheric density and measurements for Field-Aligned-Currents and low-energy particle precipitation are utilized to investigate the impacts of IP shock on NO emission during geomagnetic quiet period by using superposed epoch analysis technique.

The SABER is one of four instruments onboard the TIMED satellite, launched on December 7, 2001 (Russell et al., 1999). It asymmetrically covers the Earth, spanning latitudes from approximately 53° in one hemisphere to 83° in the other over a 60–65 days period, corresponding to the satellite's yaw period (Russell et al., 1999; Mlynczak et al., 2005). SABER is equipped with a 10-channel broadband limb-scanning infrared radiometer, which measures radiance (W. $m^{-2}.sr^{-1}$) from emissions between 1.27 µm and 16.9 µm with a vertical resolution of about 2 km. This includes the thermospheric NO emission at a wavelength of 5.3 µm (Mlynczak et al., 2003). The volume emission rate (VER) of NO is calculated from the limb radiance measurement by using an Abel's inversion technique (Mlynczak et al., 2003; 2005; 2007; Mertens et al., 2004). The vertical integration over altitudes of 100–250 km provides the cooling flux. The uncertainty in SABER's NO cooling rate measurements is better than 15 % (Mlynczak et al., 2010). We utilized SABER version 2.0 data in the present study.

Field-Aligned Currents (FACs) are obtained from the Active Magnetosphere and Planetary Electrodynamics Response Experiment (AMPERE). The AMPERE dataset provides continuous, global-scale measurements of magnetic field perturbations caused by FACs, using the Iridium satellite constellation. These measurements include both upward and downward FACs on a magnetic latitude-magnetic local time grid, with a 10-minute integration time and a 2-minute time resolution (Anderson et al., 2000; Anderson et al., 2014).

Low-energy particle flux generates NO density through a series of chemical reactions. The low-energy particle (electrons and ions) flux is obtained from the Defense Meteorological Satellite Program (DMSP) via the Madrigal database (https://cedar.openmadrigal.org). The DMSP satellites, which orbit at an altitude of 850 km with a period of about 100 min, are polar satellites in sun-synchronous orbits, covering a broad range of magnetic local times beneath them (Rich et al., 1985). The DMSP satellite are equipped with sensors that detect low-energy particles. They measure auroral precipitating particles from 30 eV to 30 keV across 20 energy channels every second with pitch angles in the loss cone. The electron and ion fluxes are divided into three energy categories: low (0.03–0.949 keV, i.e., <1 keV), mid (0.949–9.45 keV, i.e., 1 keV < E < 10 keV), and high (9.45–30 keV, i.e., >10 keV). We utilized DMSP F17 spacecraft observations for high latitude regions (latitude > 60°) in both hemispheres.

NO cooling emission depends on the densities of NO, atomic oxygen and thermospheric temperature (Mlynczak et al., 2003). In the present study, we used densities of NO, atomic oxygen and thermospheric temperature from NRLMSISE2.1 model (Emmert et al., 2022). The NRLMSISE2.1 model is an empirical atmospheric model that calculates the densities and temperatures of the Earth's atmosphere at various altitudes from the surface up to the exosphere. It takes into account different factors such as solar and geomagnetic activity, latitude, longitude, season, and time of day to provide accurate estimations of atmospheric parameters. The uncertainties in NO, Atomic oxygen, atomic nitrogen and temperature are, respectively, about ± 30–50 %, ±20-30 %, ±30-50 % and ± 10–15 K (Emmert et al., 2022).

The solar and interplanetary magnetic field (IMF) data along with Akasofu (ϵ) parameter are obtained from the WIND spacecraft located at L1 Lagrangian point (https://wind.nasa.gov). Auroral electrojet (AE) and SYM-H indices are obtained from OMNIWeb database (https://omniweb.gsfc.nasa.gov). We considered 17 IP shock events having SYM-H index greater than −30 nT within −6 hr to + 18 hr of onset. The IP shock events are obtained from Oliveira (2023) and details are provided in the supplementary file. The IP events are dominated by fast forward shock with the impact angle ranging from 130° to 164°. All data are binned into 10 min average with zero epoch hour (ZEH) corresponding to the onset of IP shock.

3. Results

Fig. 1 depicts a typical case of IP shock and corresponding changes in the solar and interplanetary magnetic field (IMF), EISCAT measured electron density, temperature, Pederson conductance, magnetic indices along with NO cooling flux and thermospheric density at 400 km during 24 November 2008. It also includes the smoothed values. The IP shock occurred at 22:29 UT and is represented by a vertical red line. The x-, y- and z- components of IMF exhibited strong fluctuations that remained elevated for more than 12 h (Fig. 1a). A significant enhancement can also be noticed in the solar wind density, speed and dynamics pressure. The solar wind speed continued to rise following the IP shock. The solar wind density and dynamic pressure peaked within three hours of onset. The Akasofu parameter maximized about 2–3 h later with the magnitude of $30x10^{11}$(W). Similarly, the EISCAT measured electron density, temperature and Pederson conductance also magnified. The electron density increased all over the altitude ranges. Both electron and ion temperature increased following IP shock. However, the response time is different for electron and ion temperature. The electron temperature reached the peak magnitudes of 3200 K after 2–3 h of onset. Whereas, the ion temperature lags behind the electron temperature by about 2 h with peak value of 3500 K. The maximum Pedersen conductance of 4.5 Siemens was recorded 5.5 h after onset. Although SYM-H index remained below −25nT, strong auroral activities are noticed. In response to IP shock, NO emission and

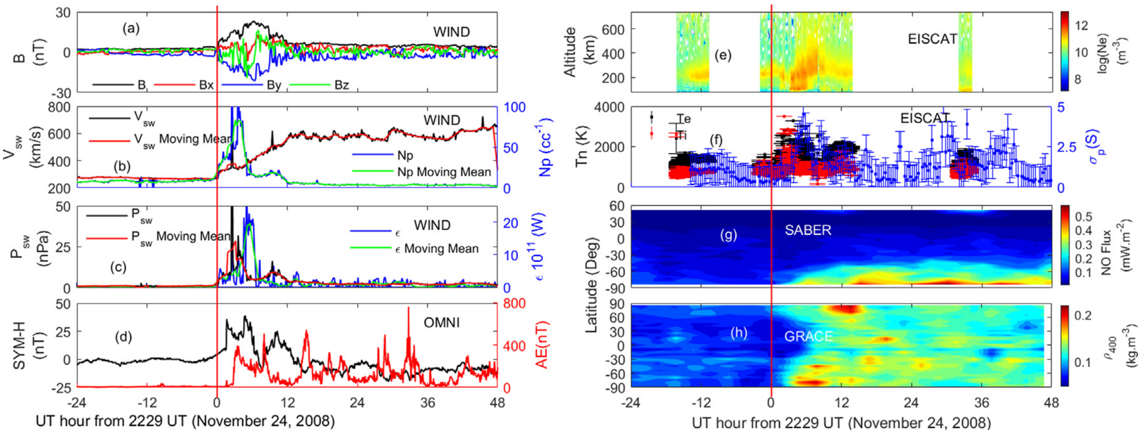

Fig. 1. Temporal variation of (a)IMF, (b) solar wind speed, (c) dynamic pressure, (d) SYM-H index, (e) electron density, (f) Ion/electron temperature and Pederson conductance, (g) NO cooling emission and (h) thermospheric density at 400 km during November 24, 2008.

thermospheric density enhanced significantly particularly in high latitude (latitude>|60°|) region. The GRACE (Gravity Recovery and Climate Experiment) satellite observations thermospheric density is normalized to 400 km using NRLMSISE00 model. About four times increase is observed in high latitude NO cooling emission with respect to pre-event value of 0.1 mW.m^{-2}. Whereas, the thermospheric density increased by double the pre-onset value. Both the cooling and density enhancements propagate towards mid- and low- latitude due to travelling atmospheric disturbances. It is more clearly noticeable in the thermospheric density. Further, it can be observed that thermospheric density responds faster to IP shock as compared to NO cooling emission.

In order to understand the average trend of solar wind parameters and corresponding cooling emission, we performed a superposed epoch analysis (SEA) with zero epoch time corresponding to onset time of IP shock. The solar wind parameter, IMF and geomagnetic indices are shown in Fig. 2. The black and red lines, respectively, represent the lower and upper quartiles. The blue lines denote the median values. The onset of IP shock is indicated by vertical red lines. The solar parameters and IMF exhibit a strong fluctuation due to IP shock. An increment is noticed in the solar wind speed, density, dynamic pressure and epsilon parameter suggest the dominance of fast forward shock. Although AE and SYM-H indices remained low, a strong auroral activity is noticed after about + 12 ZEH.

The IP shocks deposit huge amount of solar wind energy into Earth's magnetosphere. The superposed epoch analysis shows about an order increase in Epsilon parameter with respect to pre-onset value (Fig. 3a). The NO cooling emission undergoes a strong enhancement in response to the solar wind energy deposition. A global enhancement of NO emission all over the latitude sectors can be observed due to the energy deposition (Fig. 3b). A strong intensification is particularly noticeable in high latitude region that propagates towards mid- and low latitudes as time progresses. Fig. 3c shows the superposed epoch analysis of high latitude (latitude > 60°) NO emission. The

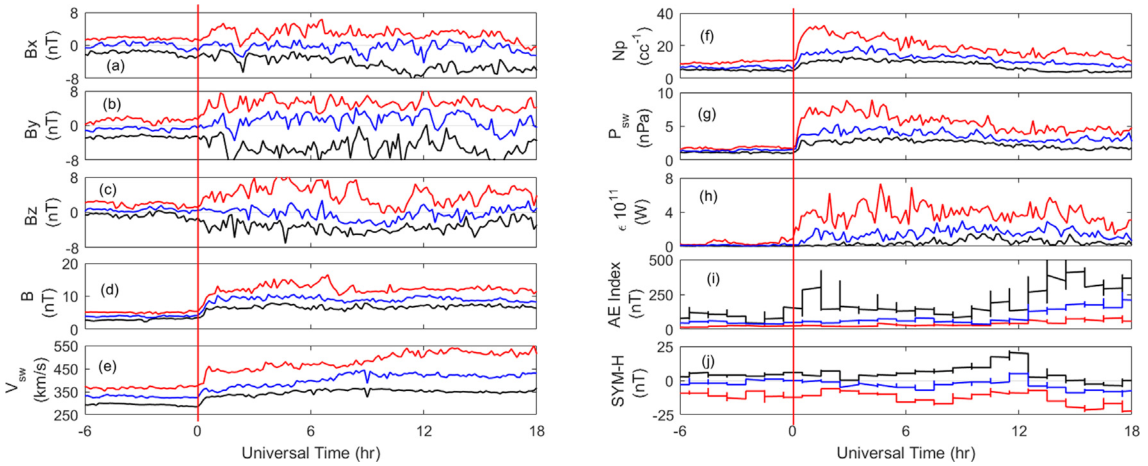

Fig. 2. Superposed Epoch study of (a) IMF Bx, (b)IMF By, (c)IMF Bz, (d)IMF average, (e)solar wind speed, (f)solar wind density, (g)solar wind dynamic pressure, (h)Epsilon parameter, (i) AE index and (j) SYM-H index. All data are binned into 10-minutes averages. Lower quartile, upper quartile and median values are, respectively, represented by black, red and blue color. Vertical red lines denote onset of IP shock.

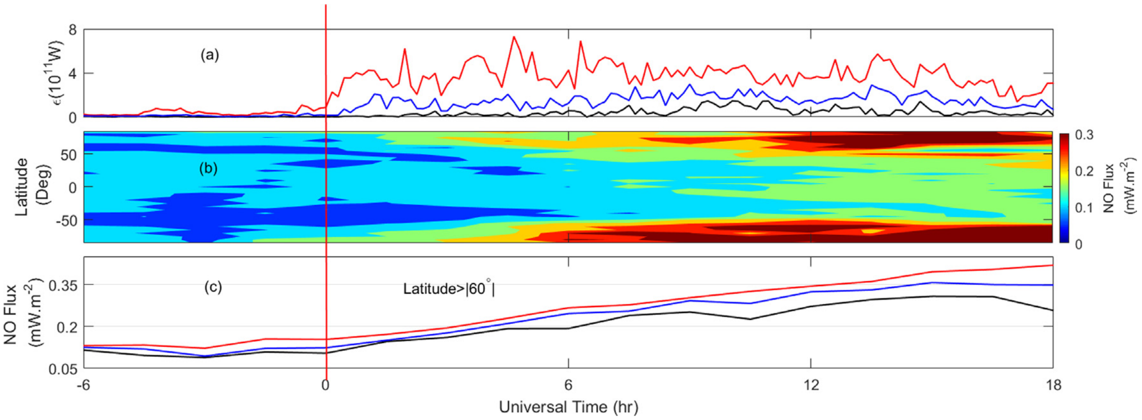

Fig. 3. Superposed epoch of (a) Epsilon parameter same as Fig. 2 (h), (b) Time-latitude cross-section NO cooling flux and (c) high latitude NO cooling flux. Lower quartile, upper quartile and median values are, respectively, represented by black, red and blue color. Vertical red lines denote onset of IP shock.

average value of NO emission was about 0.1 mW.m^{-2} during pre-event period. It increases almost linearly after the shock onset (Fig. 3c).

In order to understand the response of FACs and magnetospheric energetic particle precipitations to IP shock, Fig. 4 is presented. The upward and downward FACs, from AMPERE/Iridium satellite constellation, exhibit strong enhancements in both hemispheres. However, the enhancement in upward FACs is slightly higher than the downward current. Further, southern hemispheric FACs display a relatively higher enhancement as compared to northern hemispheric counterparts (Fig. 4a-d). The DMSP satellite observed low particle flux also demonstrates an increment during IP shock. Although both low energy electrons and ions fluxes display strong amplification due to IP shock (Fig. 4e, 4i), the particle flux of lower energy shows a stronger and earlier enhancement as compared to those of higher energy. The integrated electron flux of energy less than 1 keV shows a significant increase by about 4–5 times the pre-event value. It shows an early enhancement that peaks within about 10–12 h of onset and remains elevated for longer duration. The electron flux of higher energy (energy > 1 keV) shows a delayed response. In addition, the increase in higher energy electron flux with respect to their respective pre-event value decreases with increasing energy. Similar behavior can also be observed in the case of ion flux. However, the relative enhancement of ion flux is significantly lower than their electron counterparts. We would like to mention here that the electron flux of energy greater than ~ 10 keV displays some unexpected peaks and troughs (see Fig. 4 g-h). The detail investigation of this unexpected variation is part of future work.

The SEA study of densities of NO, N, O and thermospheric temperature are depicted in Fig. 5 as obtained from NRLMSISE2.1 model, interpolated to TIMED/SABER satellite location. We consider only high latitude (latitude > 60°) densities and temperature. The densities and temperature, respectively, correspond to the altitudes of 130 and 400 km. On average, the NO density increases twice the pre-event value (Fig. 5a). On the contrary, the

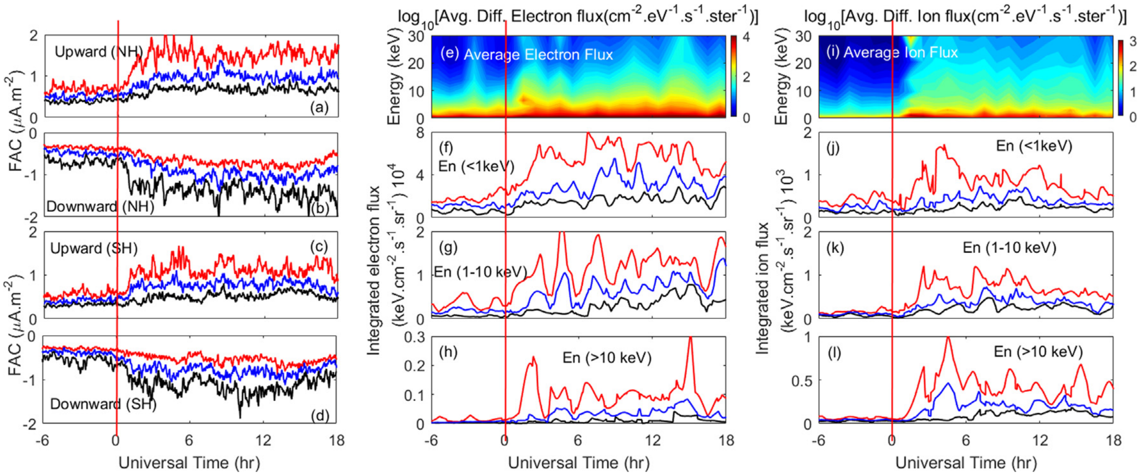

Fig. 4. Time variation of (a-d) Field-Aligned-Current, integrated (e-h) electron flux and(i-l) ion flux for different energy ranges.

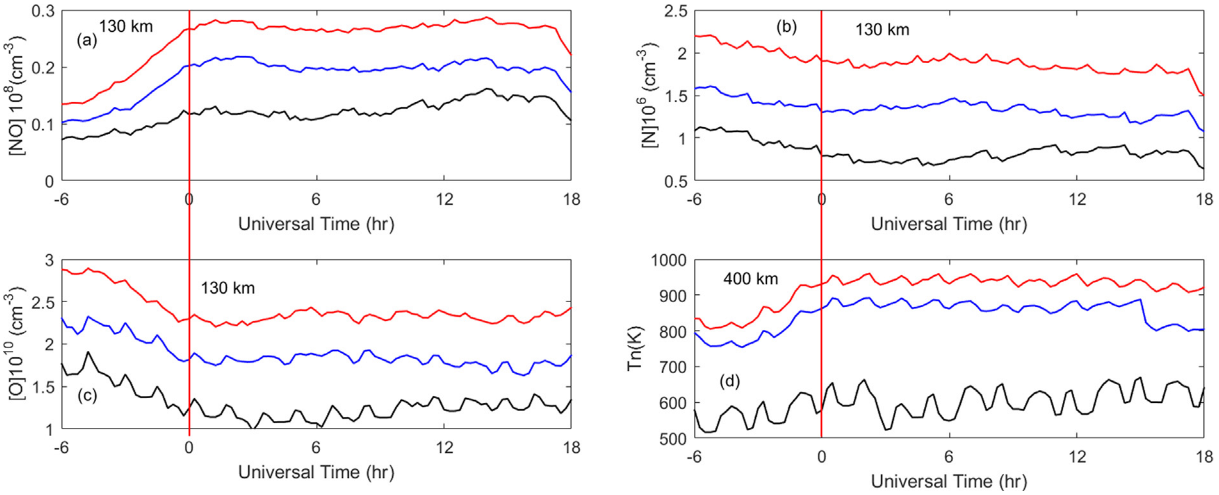

Fig. 5. Time variation of high latitude (a) NO density, (b) [N] density, (c) [O[density at 130 km and (d) thermospheric temperature at 400 km.

densities of atomic oxygen and atomic nitrogen deplete by about 40 % with respect to their pre-event values (Fig. 5b-c). A strong increase of thermospheric temperature by about 100 K is also achieved at 400 km (Fig. 5d). Both densities and temperature attempt to revert to pre-event values after about 15–16 h of onset.

4. Interpretation and discussion

The NO cooling emission strongly responds to the external energy deposition into M–I–T system. In the present study, it is observed that NO emission undergoes a strong enhancement due to IP shock even during non-geomagnetic periods. Earlier studies reported the enhancements in a high latitude FACs, particularly in the cusp region, that propagates equatorward. This enhancements in FACs are found in association with Joule heating rate (Plamroth et al., 2004; Wang et al., 2014; Shi et al., 2017;2019; Bag and Ogawa. 2024a). Further, it is well established that the IP shocks modify the size and shape of magnetosphere. The fluctuation (expansion/contraction) of the magnetosphere is known to increase the dayside magnetic reconnection and formation of discrete aurora due to particle precipitation by pitch angle diffusion and FACs (Sato et al., 2001; Fujita et al., 2004; Fujita 2019). Further, FACs exhibit a hemispheric asymmetry with higher southern hemispheric values. Similar strong hemispheric asymmetry has been reported earlier during space weather events (Bag. 2018b; Bag et al., 2020 and references therein). However, no hemispheric asymmetry has been studied during IP shock. The hemispheric difference can be attributed to the seasonal bias of the sampled events and hemispheric difference in magnetic field. The reduced southern hemispheric magnetic field would result in larger ionosphere electric field and Joule heating rate (proportional to the square of electric field).

The increase in the low energy particle precipitation impacts the ionosphere-thermosphere system (Knipp et al., 2013; Barth,2010). Earlier studies reported that electrons of 1–10 keV and ions of 10–20 keV strongly dictate the formation of NO density via a series of chemical reactions (Richardds, 2004; Barth, 2010; Barth et al., 2009). The electrons of energy less than 1 keV primarily affect the altitude above 120 km, while those higher energy influences higher altitude. The electrons of lower energy(energ y < 1 keV) have strong influence on NO cooling emission and it immediately uplifts thermospheric density (Knipp et al., 2013). The early and excessive enhancement of low energy electron flux would result in the formation of NO density which is noticeable from Figs. 4 and 5. Similar increase in particle flux, NO density and subsequent NO cooling flux during shock led geomagnetic storms has been reported by Knipp et al. (2013). An analogous variation in the particle flux, nitric density and NO cooling flux can also be observed during non-geomagnetic IP shocks periods (Figs. 2, 4-5). In addition to electron flux, ion flux also dictates the variability of NO cooling emission via production of NO density in the nocturnal atmosphere (Galand et al.,1999). Further, IP shock also generates ionospheric flow vortex and equatorward expansion of auroral boundary due to FACs which would dictate the variation of NO emission due to its non-linear dependence on ion/electron temperature (Luhr et al., 1995; Jin et al., 2023).

5. Summary

The infrared radiative emission by Nitric Oxide at 5.3 μm wavelength is the dominating coolant that effective regulates thermospheric temperature above 100 km. It strongly depends on the solar wind and magnetospheric energy deposition into Earth's atmosphere. We utilized multi-satellite observations to investigate the impacts of interplanetary (IP) shock on NO emission by using superposed epoch analysis technique. The IP shock resulted in the strong high latitude NO cooling emission. The AMPERE/Iridium satellite constellation observations of

FACs display strong enhancements in both hemispheres. However, the upward FAC is slightly higher than the downward current. Further, southern hemispheric FAC display a relatively higher enhancement as compared to northern hemispheric counterparts. The DMSP spacecraft measurement of low particle flux (energy < 1 keV) demonstrates a stronger pre-event enhancement as compared to those of higher energy. Similar variation is also observed in NO density and thermospheric temperature. NO density, at 130 km, increased by an order of magnitude as compared to the pre-event value. About 40 % decrease in atomic oxygen and atomic nitrogen densities are observed. The thermospheric temperature increased by about 100 K during IP shock period at 400 km. The strong and linear enhancement in high latitude NO cooling emission can be attributed to the huge amount of solar wind energy deposition into Earth's atmosphere due to IP shock and subsequent enhancements in FACs and particle precipitation that resulted-in the increase in NO density and thermospheric temperature.

Declaration of competing interest

The authors declare that they have no known competing financial interests or personal relationships that could have appeared to influence the work reported in this paper.

Acknowledgments

The authors acknowledge the SABER, AMPERE, DMSP and EISCAT teams for publicly providing data.

Data availability

The SABER were downloaded from the SABER website: http:saber.gats-inc.com/data.php. The solar and IMF data are obtained from WIND spacecraft via https://wind.nasa.gov/. The geomagnetic data are from OMNIWeb (https://omniweb.gsfc.nasa.gov). AMPERE Field-Aligned-Currents are obtained via https://ampere.jhuapl.edu/. DMSP particle flux are from Madrigal database via https://cedar.openmadrigal.org. EISCAT data are obtained via https://eiscat.se/.

Appendix A. Supplementary material

Supplementary data to this article can be found online at https://doi.org/10.1016/j.asr.2024.08.005.

References

Anderson, B.J. et al., 2014. Development of large-scale birkeland currents determined from the active magnetosphere and planetary electrodynamics response experiment. Geophys. Res. Lett. 41, 3017–3025. https://doi.org/10.1002/2014GL059941.

Anderson, B.J., Takahashi, K., Toth, B.A., 2000. Sensing global Birkeland currents with IridiumR engineering magnetometer data. Geophys. Res. Lett. 27 (24), 4045–4048. https://doi.org/10.1029/2000GL000094.

Bag, T., 2018a. Diurnal variation of height distributed nitric oxide radiative emission during november 2004 super-storm. J. Geophys. Res.-Space Phys. 123, 6727–6736.

Bag, T., 2018b. Local-time hemispheric asymmetry in Nitric Oxide radiative emission during geomagnetic activity. J. Geophys. Res 123, 9669–9681.

Bag, T. et al., 2020. SABER observation of storm-time hemispheric asymmetry in nitric oxide radiative emission. J. Geophys. Res. Space Phys. 126, e2020JA028849.

Bag, T. et al., 2023a. Distinctive response of thermospheric cooling to ICME and CIR driven geomagnetic storms. Front. Astron. Space Sci. 10. https://doi.org/10.3389/fspas.2023.1107605.

Bag, T. et al., 2023b. Thermospheric NO Cooling during an unusual geomagnetic storm of 21–22 January 2005: A comparative study between TIMED/SABER measurements and TIEGCM simulations. Atmosphere 14, 556.

Bag, T., Ogawa, Y., 2024a. Enhanced response of thermospheric cooling emission to negative pressure pulse. Sci Rep 14, 9647. https://doi.org/10.1038/s41598-024-60471-2.

Bag, T., Ogawa, Y., 2024b. Response time of Joule heating rate and nitric oxide cooling emission during geomagnetic storms: Correlated ground-based and satellite observations. J. Geophys. Res.-Space Physics. 129. https://doi.org/10.1029/2023JA032072 e2023JA032072.

Barth, C.A. et al., 2009. Joule heating and nitric oxide in the thermosphere. J. Geophys. Res. 114. https://doi.org/10.1029/2008JA013765, A05301.

Barth, C.A., 2010. Joule heating and nitric oxide in the thermosphere. J. Geophys. Res. 115. https://doi.org/10.1029/2010JA015565 A10305.

Belakhovsky, V.B. et al., 2017. Geomagnetic and ionospheric response to the interplanetary shock on January 24, 2012. Earth Planets Space 69, 105.

Bharti, G. et al., 2018. Storm-time variation of radiative cooling by Nitric Oxide as observed by TIMED-SABER and GUVI. J. Geophys. Res.-Space Phys. 123, 1500–1514.

Boudouridis, A. et al., 2004a. Evaluation of the Hill-Siscoe transpolar potential saturation model during a solar wind dynamic pressure pulse. Geophys. Res. Lett. 31, L23802.

Boudouridis, A. et al., 2004b. Magnetospheric reconnection driven by solar wind pressure fronts. Ann. Geophys. 22, 1367–1378.

Boudouridis, A. et al., 2005. Enhanced solar wind geoeffectiveness after a sudden increase in dynamic pressure during southward IMF orientation. J. Geophys. Res. 110, A05214.

Bowman, B. R., et al. 2008. A new empirical thermospheric density model JB2008 using new solar and geomagnetic indices, AIAA 2008–6438. Astrodynamic Specialist Conference, Honolulu, HI.

Burlaga, L.F., 1995. Interplanetary magnetohydrodynamics. Oxford University Press.

Cao, J.B. et al., 2013. Relations of the energetic proton fluxes in the central plasma sheet with solar wind and geomagnetic activities. J. Geophys. Res. Sp. Phys. 118, 7226–7236.

Chen, X. et al., 2023. Propagation of the interplanetary shock induced pulse: New observations by the global navigation satellite system. J. Geophys. Res. Space Phys. 128. https://doi.org/10.1029/2022JA030975, e2022JA030975.

Connor, H.J. et al., 2014. The relation between transpolar potential and reconnection rates during sudden enhancement of solar wind dynamic pressure: OpenGGCM-CTIM results. J. Geophys. Res.: Space Phys. 119, 3411–3429. https://doi.org/10.1002/2013JA019728.

Emmert, J.T. et al., 2022. NRLMSIS 2.1: An empirical model of nitric oxide incorporated into MSIS. J. Geophys. Res. Space Phys. 127 e2022JA030896.

Fang, X., Thayer, J.P., Knipp, D.J., 2023. Impact of interplanetary shocks on thermospheric dynamics and Joule heating. J. Geophys. Res.: Space Phys. 128 (3), 2123–2145.

Fu, H.S. et al., 2011. Electron loss and acceleration during storm time: The contribution of wave-particle interaction, radial diffusion, and transport processes. J. Geophys. Res. 116. https://doi.org/10.1029/2011JA016672, A10210.

Fujita, S. et al., 2004. A numerical simulation of a negative sudden impulse. Earth Planets Sp. 56, 463–472.

Fujita, S., 2019. Response of the magnetosphere-ionosphere system to sudden changes in solar wind dynamic pressure. Rev. Mod. Plasma Phys. 3 (2), 2.

Galand, M. et al., 1999. Ionization by energetic protons in thermosphere–ionosphere electrodynamics general circulation model. J. Geophys. Res. 104 (A12), 27973–27989.

Gkioulidou, M., Kistler, L.M., Spence, H.E., 2022. Ion temperature and vortex dynamics during interplanetary shock events. J. Geophys. Res.: Space Phys. 127 (8), 5689–5702.

Hartinger, M.D. et al., 2022. ULF wave modeling, effects, and applications: Accomplishments, recent advances, and future. Front. Astron. Space Sci. 9. https://doi.org/10.3389/fspas.2022.867394.

Jin, Y. et al., 2023. Ionospheric flow vortex induced by the sudden decrease in the solar wind dynamic pressure. J. Geophys. Res. 128, e2023JA031690.

Knipp, D. et al., 2013. Thermospheric damping response to sheath-enhanced geospace storms. Geophys. Res. Lett. 40, 1263–1267.

Kockarts, G., 1980. Nitric oxide cooling in the terrestrial atmosphere. Geophys. Res. Lett. 7 (2), 137–140.

Li, Z. et al., 2018. A comparison study of NO cooling between TIMED/SABER measurements and TIEGCM simulations. J. Geophys. Res.: Space Phys. 123, 8714–8729.

Liu, J. et al., 2023. Transient response of polar-cusp ionosphere to an interplanetary shock. J. Geophys. Res.: Space Phys. 128 (3), e2022JA030565.

Lu, G. et al., 2018. Ionospheric consequences of interplanetary shocks: statistical study. J. Geophys. Res.: Space Phys. 123 (12), 10395–10407.

Lui, A.T.Y., 2011. Interplanetary Shocks: Observations, Mechanisms, and Consequences. Springer Science and Business Media.

Mertens, C.J. et al., 2004. SABER observations of mesospheric temperatures and comparisons with falling sphere measurements taken during the 2002 summer MaCWAVE campaign. Geophys. Res. Lett. 31, L03105. https://doi.org/10.1029/2003GL018605.

Mlynczak, M. et al., 2003. The natural thermostat of nitric oxide emission at 5.3 μm in the thermosphere observed during the solar storms of April 2002. Geophys. Res. Lett. 30 (21), 2100. https://doi.org/10.1029/2003GL017693.

Mlynczak, M.G. et al., 2005. Energy transport in the thermosphere during the solar storms of April 2002. J. Geophys. Res. 110. https://doi.org/10.1029/2005JA011141 A12S25.

Mlynczak, M.G. et al., 2010. Observations of infrared radiative cooling in the thermosphere on daily to multiyear timescales from the TIMED/SABER instrument. J. Geophys. Res. 115, A03309. https://doi.org/10.1029/2009JA014713.

Ober, D.M. et al., 2006. MHD simulation of the transpolar potential after a solar-wind density pulse. Geophys. Res. Lett. 33, L04106. https://doi.org/10.1029/2005GL024655.

Oliveira, D., 2017. Magnetohydrodynamic shocks in the interplanetary space: A theoretical review. Braz. J. Phys. 47 (1), 81–95.

Oliveira, D.M., 2023. Geoeffectiveness of interplanetary shocks controlled by impact angles: past research, recent advancements, and future work. Front. Astron. Space Sci. 10. https://doi.org/10.3389/fspas.2023.1179279.

Oliveira, D., Raeder, J., 2014. Effects of interplanetary shock impact angles on the occurrence of ultra-low frequency waves. Front. Astron. Space Sci. 1, 23.

Oliviera et al., 2024. (2024), First direct observations of interplanetary shock impact angle effects on actual geomagnetically induced currents: The case of the Finnish natural gas pipeline system. Front. Astron. Space Sci. 11. https://doi.org/10.3389/fspas.2024.1392697.

Palmroth, M. et al., 2004. Role of solar wind dynamic pressure in driving ionospheric Joule heating. J. Geophys. Res. 109. https://doi.org/10.1029/2004JA010529, A11302.

Rae, I.J., Murphy, K.R., Mann, I.R., 2022. Field-aligned currents and auroral intensification during interplanetary shocks. Geophys. Res. Lett. 49 (5) e2022GL097863.

Richards, P.G., 2004. On the increases in nitric oxide density at midlatitudes during ionospheric storms. J. Geophys. Res. 109, A06304. https://doi.org/10.1029/2003JA010110.

Russell III, J. M, et al. 1999. An overview of the SABER experiment and preliminary calibration results. Paper presented at SPIE Conference on Optical Spectroscopic Techniques and Instrumentation for Atmospheric and Space Research III. SPIE Vol. 3756, Denver, Colorado, July 1999.

Sato, N. et al., 2001. Enhancement of optical aurora triggered by the solar wind negative impulse (SI$^-$). Geophys. Res. Lett. 28, 127–130.

Schiller, Q. et al., 2016. Prompt injections of highly relativistic electrons induced by interplanetary shocks: A statistical study of Van Allen Probes observations. Geophys. Res. Lett. 43, 12317–12324.

Shi, Y. et al., 2017. High-latitude thermosphere neutral density response to solar wind dynamic pressure enhancement. J. Geophys. Res.: Space Phys. 122, 11559–11578.

Shi, Y. et al., 2019. Effects of Nearly Frontal and Highly Inclined Interplanetary Shocks on High-latitude Field-aligned Currents (FACs). Space Weather 17, 1659–1673.

Turner, D.L., Claudepierre, S.G., Blake, J.B., 2021. The role of interplanetary shocks in magnetospheric dynamics: A comprehensive review. Space Sci. Rev. 217 (1), 23.

Wang, H. et al., 2014. Strong ionospheric field-aligned currents for radial interplanetary magnetic fields. J. Geophys. Res. Space Physics 119, 3979–3995.

Yue, C. et al., 2010. Geomagnetic activity triggered by interplanetary shocks. J. Geophys. Res. 115, 1–13.

Zhou, X.Y. et al., 2003. Shock aurora: FAST and DMSP observations. J. Geophys. Res. 108 (A4), 8019. https://doi.org/10.1029/2002ja009701.